Practical Limitations of Aerosol Separation by a Tandem Differential Mobility Analyzer-Aerosol Particle Mass Analyzer

James G. Radney and Christopher D. Zangmeister

Material Measurement Laboratory, National Institute of Standards and Technology, Gaithersburg, Maryland, 20899, USA

Address Correspondence to Christopher Zangmeister, National Institute of Standards and Technology, 100 Bureau Dr., Gaithersburg, MD 20899. E-mail: cdzang@nist.gov

Color versions of one or more of the figures in the article can be found online at www.tandfonline.com/uast.

Running Title: Practical Limitations of DMA-APM Separation

ABSTRACT

A cavity ring-down spectrometer and condensation particle counter were used to investigate the limitations in the separation of singly and multiply charged aerosol particles by a tandem differential mobility analyzer (DMA) and aerosol particle mass analyzer (APM). The impact of particle polydispersity and morphology was investigated using three materials: nearly-monodisperse polystyrene latex nanospheres (PSL); polydisperse, nearly-spherical ammonium sulfate (AS) and polydisperse lacey fractal soot agglomerates. PSL and AS particles were easily resolved as a function of charge. For fresh soot, the presence of multiply charged particles severely affects the isolation of the singly charged particles. In cases where the DMA-APM was unable to fully resolve the singly charged particles of interest, the peak mass deviated by up to 13 % leading to errors in the mass specific extinction cross section of over 100 %. For measurements of non-spherical particles, non-symmetrical distributions of concentration as a function of mass were a sign of the presence of multiply charged particles. Under these conditions, the effects of multiply charged particles can be reduced by using a second charge neutralizer after the DMA and prior to the APM. Dilution of the aerosol stream serves to decrease the total number concentration of particles and does not remove the contributions of multiply charged particles.

1. INTRODUCTION

The use of a tandem differential mobility analyzer (DMA), aerosol particle mass analyzer (APM) coupled to a condensation particle counter (CPC) to measure aerosol mass distributions has been extensively documented in the literature (Barone et al. 2011; Charvet et al. 2014; Cross et al. 2010; Geller et al. 2006; Kuwata and Kondo 2009; Laborde et al. 2012; Lall et al. 2009; Lall et al. 2008; Lee et al. 2011; Lee et al. 2009; Lin et al. 2014; Ma et al. 2013a; Ma et al. 2013b; Malloy et al. 2009; Olfert and Collings 2005; Olfert et al. 2006; Pagels et al. 2009; Park et al. 2003a; Park et al. 2004b; Park et al. 2003b; Rissler et al. 2013; Sakurai et al. 2003; Scheckman et al. 2009; Shin et

al. 2010; Tajima et al. 2011; Tajima et al. 2013; Xue et al. 2009). Some studies have added optical measurements to afford an additional level of classification (Radney et al. 2013; Radney et al. 2014). DMAs size-select particles by electrical mobility (Knutson and Whitby 1975) while APMs mass-select particles based on the balance of centrifugal and electrostatic forces (Ehara et al. 1996). Both methods use net charge in the mechanism of particle classification. Prior studies have only considered particles bearing a single net charge (Barone et al. 2011; Lall et al. 2008; Lin et al. 2014; Olfert 2005; Tajima et al. 2011; Tajima et al. 2013). A recent modeling study by (Kuwata 2015) did consider the effects of multiply charged particles in a tandem DMA-APM measurement. However, only a single combination of transfer functions was considered for a given set of conditions instead of the convolution of transfer functions as is required; see ensuing discussion or (Lall et al. 2009). Other measurement studies have demonstrated the presence of particles with multiple charges, but did not offer implications as to how they may affect subsequent measurements (Charvet et al. 2014; Lee et al. 2011; Radney et al. 2013). A detailed investigation on the classification of particles using the tandem DMA-APM technique as a function of net charge is warranted. Here, we provide an in-depth study on particles bearing multiple charges and the resultant effects on the interpretation of mass, number concentration, and extinction measurements and the calculated extinction cross sections using 3 aerosols with different properties: polystyrene latex nanospheres (PSL), ammonium sulfate (AS) and fresh soot. Polystyrene latex nanospheres are monodisperse and spherical while ammonium sulfate is polydisperse and nearly-spherical. Fresh soot is polydisperse and non-spherical comprised of lacey aggregates with low effective density and high void volume. Studying these three materials enables the effect of polydispersity and morphology on the tandem DMA-APM separation to be studied and potential resolution limitations to be elucidated.

2. THEORY

Particles suspended in a flowing gas stream are subjected to low-speed drag forces that will affect their electrostatic, diffusive and inertial properties. Assuming laminar flow conditions (i.e. low Reynolds number) and slow particle rotation (relative to a background fluid), the drag force ($\vec{F}_{\mathrm{Drag}}$) can be written as

$$\vec{F}_{\mathrm{Drag}} = f\left(\vec{u}_{\mathrm{f}} - \vec{u}_{\mathrm{p}}\right) \quad (1)$$

where $\vec{u}_{\mathrm{f}}$ and $\vec{u}_{\mathrm{p}}$ represent the fluid and particle velocity vectors, respectively (Zhang et al. 2012). From the semi-empirical Stokes-Millikan equation, the friction coefficient (*f,* units of g s^{-1}) for spherical particles can be written as

$$f = \frac{3\pi\mu D}{C(\mathrm{Kn})} \quad (2)$$

where μ, D and C(Kn) are the gas dynamic viscosity, particle diameter and the Cunningham slip correction factor, respectively. The Cunningham slip correction factor is

$$C(\mathrm{Kn}) = 1 + \mathrm{Kn}\left(\alpha + \beta e^{-\gamma/\mathrm{Kn}}\right) \quad (3)$$

where Kn is the Knudsen number (Kn = $2\lambda_{\mathrm{MFP}}$/D, λ_{MFP} = gas mean free path) and α, β, and γ are constants with values of 1.142, 0.558 and 0.999 in air, respectively (Allen and Raabe 1985). The Cunningham slip correction factor has been included in Eq. 2 to account for the fact that the friction coefficient is less than would be predicted by Stoke's Law as aerosols occupy the free molecular and transition regimes (Kn > 0.25). For particles in the continuum regime, C(Kn) → 1. Previous investigations have modeled the friction coefficient of non-spherical aggregates in the free molecular and transition regime and some have a similar form to Eq. 2 except that D – and hence

Kn and C(Kn) – are based upon the projected area of the particle (Gopalakrishnan et al. 2011; Hogan and de la Mora 2011; Melas et al. 2014; Zhang et al. 2012). Other investigations have used the functional form

$$f = AN^{\eta} \quad (4)$$

where A is a constant related to the friction coefficient of a single monomer (f in Eq. 1), N is the number of monomers and η is the power law dependence of f on N (Chan and Dahneke 1981; Isella and Drossinos 2010; Mackowski 2006; Meakin et al. 1989; Shin et al. 2009). For ideal aggregates, $\eta = 1$, but due to shielding effects in real particles $\eta < 1$.

2.1. DMA Separation

Differential mobility analyzers separate aerosols based upon particle mobility within an electric field (Z_p) (Knutson and Whitby 1975) in a bath gas of known composition. When aerosol inlet and outlet flows are equal,

$$Z_p = \frac{qe}{f} = \frac{q_{sh}}{2\pi VL} \ln\left(\frac{r_2}{r_1}\right) \quad (5)$$

where q is the number of charges on the particle, e is the elementary charge (1.602 x 10^{-19} C) and f is the friction coefficient in Eq. 1 , 2 and 4. Electrical mobility can be related to the physical properties of the DMA column through the right-hand side of Eq. 5 where q_{sh}, V, L, r_1 and r_2 are the volumetric sheath flow rate, the average voltage applied to the inner electrode, the length of the classification area and the radii of the inner and outer (grounded) electrodes, respectively.

From this point forward, we will use D_m, the mobility diameter of the particle, instead of D, the physical diameter, to represent particle diameter. For aggregated particles, a physical diameter cannot be defined as the particles are non-spherical. However, we can measure the mobility of an aggregated particle in an electric field and relate that to spherical particles with known diameter as defined in Eq. 5. This gives us a direct comparison between particles of different morphologies even though the absolute definition of D_m is rather loose.

From Eq. 5, it is evident that for a given Z_p, a single unique solution does not exist; i.e. multiple values of q/f (and hence D_m) can satisfy this relationship. In practice, multiple charging effects can be reduced by either working at Z_p values where particles with larger D_m are minimal (Cross et al. 2010) or applying an inversion algorithm, as discussed in (Wiedensohler et al. 2012).

The electrical mobility bandwidth (ΔZ_p) is

$$\Delta Z_p = \frac{q_a}{q_{sh}} Z_p \quad (6)$$

where q_a is the aerosol volumetric flow rate. The transfer function of the DMA (Ω_{DMA}) can be described as an isosceles triangle with value of 1 at Z_p and going to 0 at $Z_p \pm \Delta Z_p$ for conditions where the aerosol inlet and outlet flows are equal (Kinney et al. 1991); see Fig. 1a and 1e.

2.2. APM Separation

Aerosol particle mass analyzers separate particles based upon the balance of centrifugal and electrostatic forces within a rotating annular region that can be described by (Ehara et al. 1996)

$$m_p r\omega^2 = \frac{qeV}{r\ln(r_2/r_1)} \quad (7)$$

where m_p and ω are the mass of the particle and the angular rotation speed, respectively; V, r_2 and r_1 have the same definition as for the DMA. The value r represents the radius of the center of the annular classification space; i.e. $r = {(r_1 + r_2)}/{2}$. Similar to the DMA, a unique solution for m_p/q does not exist for a given ω and V. For the APM, this results in the effective mass (m_{eff}) of the particle being measured when $q > +1$ where

$$m_{eff} = \frac{m_p}{q} \tag{8}$$

For the APM used in this study, we can define the classification parameter (λ_c) (Ehara et al. 1996)

$$\lambda_c = \frac{2\tau\omega^2 L}{v_0} \tag{9}$$

where L and v_0 are the length of the classification region and volumetric flow rate, respectively. The quantity τ is the relaxation time and is equal to m_p/f where f is the friction coefficient in Eq. 1, 2 and 4. The classification parameter represents the ratio of radial to axial transversal times and is a measure of the APM's separation ability. Higher values values of λ_c yield better resolution but lower particle throughput.

The use of a tandem DMA-APM system allows for the determination of effective density (ρ_{eff}) where

$$\rho_{eff} = \frac{6}{\pi}\frac{m_p}{D_m^3} \tag{10}$$

For spherical particles, the effective and bulk densities should be equal. However, in practice the effective density is less than the bulk density due to non-sphericity or air inclusions. If a collection of mobility diameter and mass pairs are measured the mass-mobility scaling exponent (D_{fm}) can be calculated using

$$m_p = k_0 \left(\frac{D_m}{150\ \text{nm}}\right)^{D_{fm}} \tag{11}$$

where k_0 is the particle mass at a reference particle size (150 nm used in this investigation). The mass-mobility scaling exponent is a commonly used metric for particle morphology; spherical particles will have $D_{fm} \approx 3$ while non-spherical particles will have $D_{fm} < 3$ (Ma et al. 2013a; McMurry et al. 2002; Park et al. 2004a; Rissler et al. 2013). Fractal aggregates, such as soot, typically have $1.8 \leq D_{fm} \leq 2.2$.

If only a single charge is considered, as in(Lall et al. 2009), (Tajima et al. 2011) and (Tajima et al. 2013), the theoretical separation by a tandem DMA-APM, can be seen schematically in Fig. 1a through 1d; for the present discussion we have assumed that particles do not possess a distribution of effective densities for a given electrical mobility. Particles with a given electrical mobility (Z_p) and electrical mobility bandwidth (ΔZ_p), and hence mobility diameter (D_m), are selected by the DMA with the transfer function (Ω_{DMA}) shown in Fig. 1a. Particles within $Z_p \pm \Delta Z_p$ pass through the DMA to the APM. The APM possesses its own inherent transfer function and, ideally, particles within ΔZ_p (gray dotted lines in Fig. 1a) map directly to their respective masses. Instead particles can map to a range of masses as seen by the green traces in Fig 1b. (Each gray dotted line in Fig. 1a corresponds to a separate trace in Fig. 1b). This broadening arises from the multitude of flow vectors a particle can traverse depending upon the radial position (r) at which it enters the annular region. Lower values of the classification parameter (λ_c) increase this broadening. Thus, a superposition of the individual APM and DMA transfer functions ($\Omega_{DMA}\Omega_{APM}$, green lines Fig. 1c) occurs. The superposition term represents the effective penetration of a given particle with a specific Z_p at a specific m_p. The actual theoretical output of the APM is the summation of all the

individual transfer functions and is shown as the red line in Fig. 1c. Finally, the number concentration of particles that exits the DMA-APM, relative to the number concentration that entered, to be measured by a downstream CPC also depends upon the Boltzmann charge distribution (P_q) imparted by the charge neutralizer (Wiedensohler and Fissan 1988) and is shown in Fig. 1d.

The objective of this manuscript is to demonstrate limitations of using a DMA-APM when particles with higher order charges are considered as in Fig. 1e) through 1h). We note that throughout the remainder of this manuscript, the coloring convention shown in Fig. 1 will be maintained; q = +1, +2 and +3 will be shown in green, cyan and blue, respectively, while the summation of the contributions from all charges will be shown in red. We present measurements of polystyrene latex nanospheres, ammonium sulfate and flame generated soot to demonstrate the presence of multiply charged particles within a mass distribution and provide guidelines for the interpretation of mass separation under experimental conditions. Beyond measuring number concentration using a condensation particle counter (CPC), as is commonly performed, we also measure particle extinction to aid in the identification of particles by charge from their extinction cross sections; i.e. larger particles with multiple charges will have significantly larger extinction cross sections. We conclude by presenting a framework to identify the presence of multiply charged particles and reduce their impact on measurement quality and interpretation.

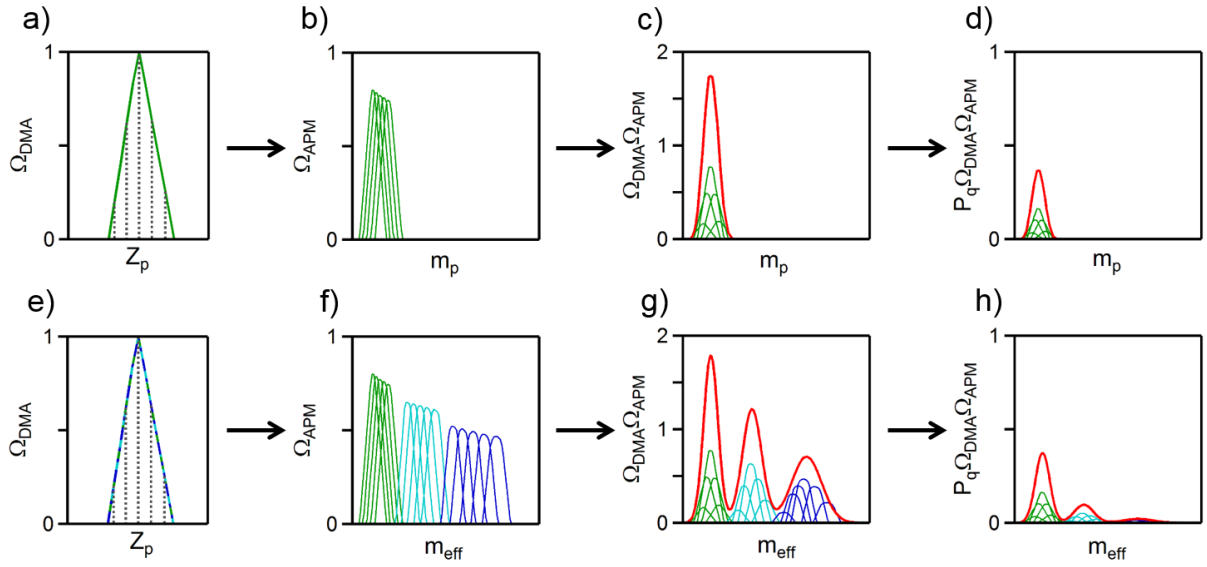

Figure 1: Schematic of the theoretical transfer functions and separation of aerosol particles at an electrical mobility (Z_p) and mass (m_p) combination using a tandem DMA and APM. Panel a), b), c) and d) represent the transfer function of the DMA (Ω_{DMA}), the transfer function of the APM (Ω_{APM}), the convolution of DMA and APM transfer functions (Ω_{DMA} Ω_{APM}) and the convoluted transfer function after being weighted to the appropriate Boltzmann charge distribution (P_q) from the charge neutralizer, respectively, when only particles bearing a single charge are considered. Each green trace in b) through d) corresponds to one of the gray dotted lines in a). The solid red lines in c) and d) correspond to the summation of all of the individual transfer functions. Panels e) through h) follow the same progression as a) through d) except that the contributions of multiply charged particles have been included and are shown in cyan (q = +2) and blue (q = +3). These 3 traces are overlapped in e) because they possess identical electrical mobility values, see

Eq. 5 and discussion in text. In b) through d), distributions are plotted against m_p since $q = +1$ while in f) through h) distributions are plotted against m_{eff} as $q > +1$ are present.

3. MATERIALS & METHODS

A block diagram of the experimental setup used presently is shown in Fig. 2.

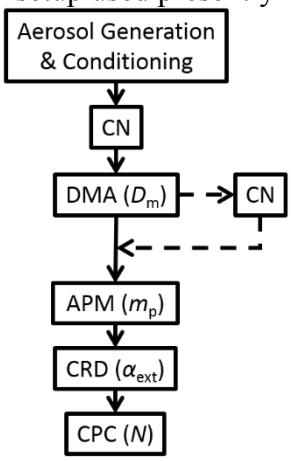

Figure 2: Schematic of the experimental setup used in this study. Solid lines indicate primary flows and dashed lines indicate optional flows. Measured quantities are shown in parenthesis. Abbreviations: charge neutralizer (CN), differential mobility analyzer (DMA), aerosol particle mass analyzer (APM), cavity ring-down spectrometer (CRD) and condensation particle counter (CPC).

3.1. Polystyrene Latex Nanospheres Generation

Polystyrene latex nanospheres (PSL) aerosol with nominal diameters of 102 ± 3 nm (Thermo Scientific 3100A)[1], 147 ± 3 nm (Thermo Scientific 3150A) and 203 ± 5 nm (Thermo Scientific 3200A) were generated from aqueous solutions at a concentration of 2 drops mL^{-1} using a constant-output liquid jet cross flow atomizer (TSI 3096, 30 psig) operated on particle-free air supplied by an FT-IR purge gas generator (dew point < -73 °C). Of the ≈ 2.2 L min^{-1} of flow, 0.5 L min^{-1} was conditioned by passing the aerosol laden stream through a pair of diffusion dryers (TSI 3602). Excess flow was exhausted into a fume hood.

3.2. Ammonium Sulfate Generation

Ammonium sulfate (AS) aerosol was generated from 1 mg mL^{-1} aqueous solution similarly to the PSLs except that the aerosol stream was passed through a tube furnace (Lindberg-Blue Mini Mite) at 150 ^{0}C in between the pair of diffusion dryers.

3.3. Soot Generation

Soot was generated using a Santoro diffusion flame operated on ethylene fuel (Santoro et al. 1983). Soot was sampled at 5 cm above the base of the flame along the centerline and aspirated into a 4 L min^{-1} carrier stream of dry, HEPA-filtered air. An ejector pump situated downstream of

[1]NIST Technical Disclaimer: Certain commercial equipment, instruments, or materials (or suppliers, or software, ...) are identified in this paper to foster understanding. Such identification does not imply recommendation or endorsement by the National Institute of Standards and Technology, nor does it imply that the materials or equipment identified are necessarily the best available for the purpose.

the sampling port was operated at 8 L min^{-1} using dry, HEPA-filtered air. Of the ≈ 12 L min^{-1} of total flow, 0.5 L min^{-1} was sampled for further analysis and conditioned similarly to the AS. Excess flow was exhausted in a fume hood.

3.4. Cavity Ring-down Spectroscopy

The use of cavity ring-down spectroscopy (CRDS) for the measurement of aerosol extinction coefficients has been well documented in the literature, so only a brief description will be given presently. For more details, the reader is directed to Atkinson's review on CRDS for environmental applications (Atkinson 2003). Light from a λ = 660 nm laser pumps a high finesse optical cavity to saturation (mirror reflectivity > 99.98 %, transmission ≈ 0.002 %). The light intensity is quickly terminated using an acousto-optic modulator. The intensity of light in the cavity decays passively and exponentially through mirror loss, absorption by gas molecules, and the scattering and absorption of light by aerosols; extinction is the sum of scattering and absorption. Mathematically, this process is described by

$$I = I_0 e^{-c\alpha_{\text{ext}}t} \tag{12}$$

where I_0 and I are the initial light intensity and the intensity at time t, respectively, c is the speed of light and α_{ext} is the extinction coefficient (units of m^{-1}) which corresponds to the fractional loss of light intensity due to extinction per unit distance. The quantity $c\alpha_{\text{ext}}$ represents the decay rate. Aerosol extinction coefficients are calculated by taking the difference in measured extinction coefficients between aerosol laden and HEPA-filtered air streams

$$\alpha_{\text{ext,aerosol}} = \alpha_{\text{ext,total}} - \alpha_{\text{ext,HEPA}} \tag{13}$$

In the present setup, ring-downs are measured at 100 Hz and then averaged to 1 s; typical ring-down times for the HEPA-filtered air were ≈ 26 x 10^{-6} s. These data points were then averaged to 5 s. At this averaging interval, the minimum uncertainty, as calculated from an Allan deviation (Sullivan et al. 1990), is 1.3 x 10^{-7} m^{-1} corresponding to a limit of detection (LOD, 3 times the minimum uncertainty) of 3.9 x 10^{-7} m^{-1}.

3.5. Aerosol Mass Distribution Measurements

The distribution of extinction and number concentration as a function of mass were measured by the CRD and CPC, respectively, as in (Radney et al. 2013) and (Radney et al. 2014). The DMA was operated with an aerosol flow of 0.5 L min^{-1} and sheath flow of 5.0 L min^{-1}. Measurements were made with the APM set to the desired rotation speed corresponding to a $\lambda_c = 0.32$ and a peak mass density of 1.05 g cm^{-3}, 1.77 g cm^{-3} and 0.15 g cm^{-3} for the PSL, AS and soot, respectively. The APM was continuously scanned for 10 min over the mass range of interest with rotation speed, voltage and number concentration being logged at 100 Hz and then average to 1 s; in post-processing data was averaged to 5 s. For the soot experiments using multiple charge neutralizers, data was binned to 5 x 10^{-17} g as 6 x 10 min mass distributions were collected over separate voltage windows (at a common rotation speed) in order to improve the mass resolution as the program controlling the APM ramps the voltage exponentially to mimic a scanning DMA (Collins et al. 2004). This exponential ramp can increase broadening in the mass distribution and shift the observed peak mass when sufficiently wide mass windows are needed.

From the number concentration and extinction mass distributions, the extinction cross section (C_{ext}) of each data point in the mass distribution was calculated as

$$C_{\text{ext}} = \frac{\alpha_{\text{ext}}}{N} \quad (14)$$

in order to isolate particles by charge from the change in slope in the plot of C_{ext} vs m_{p}, see Figure 3d and corresponding discussion.

4. RESULTS & DISCUSSION

4.1. Polystyrene latex nanospheres

Polystyrene latex spheres were used to first validate measurements of mass, number concentration, extinction and extinction cross section. PSLs represent a nearly ideal test particle for the tandem DMA-APM measurements as they are spherical and nearly monodisperse with a well-defined size, mass, density (ρ = 1.05 g cm^{-3}) and refractive index; n = 1.5855 as extrapolated from (Sultanovaa et al. 2009). Particles with nominal diameters of 102 ± 3 nm, 147 ± 3 nm and 203 ± 5 nm were analyzed. Mass distributions for the 147 nm PSLs are shown in Figure 3a through 3d as a function of number concentration (N) on a linear axis, number concentration (N) on a logarithmic axis, extinction (α_{ext}) and extinction cross section (C_{ext}), respectively. Mass distributions for the 102 nm and 203 nm PSLs can be found in Fig. S1 and S2 of the Supporting Information. For all PSLs measured, the DMA was set to the nominal diameter; Z_{p} = 2.5994 x 10^{-8} m^2 V^{-1} s^{-1}, 1.4010 x 10^{-8} m^2 V^{-1} s^{-1}, and 8.4106 x 10^{-9} m^2 V^{-1} s^{-1} for the 102, 147 and 203 nm respectively. For all data sets, number concentration data has been plotted on both linear and logarithmic axes – Fig. a and b, respectively – to highlight the small absolute contribution to number concentration and the larger relative contribution to extinction by particles bearing higher order charges, respectively. Shaded gray areas correspond to the 2σ measurement uncertainty at this 5 s temporal resolution. The data for N and α_{ext} show that for the PSL, the q = +1 particle is well separated from others present in the distribution. In the plot of extinction cross section (Fig. 3d), well separated particles can be recognized as regions with a continuous and nearly constant slope where particles bearing the unique charge are present. In Fig. 3 this corresponds to the nearly flat sections around ≈ 2.0 x 10^{-15} g and 3.25 x 10^{-15} g. When there is overlap between the different particles, there is a sharp change in the slope of C_{ext} which is indicative of a transition region where particles of different charge and/or morphologies being present.

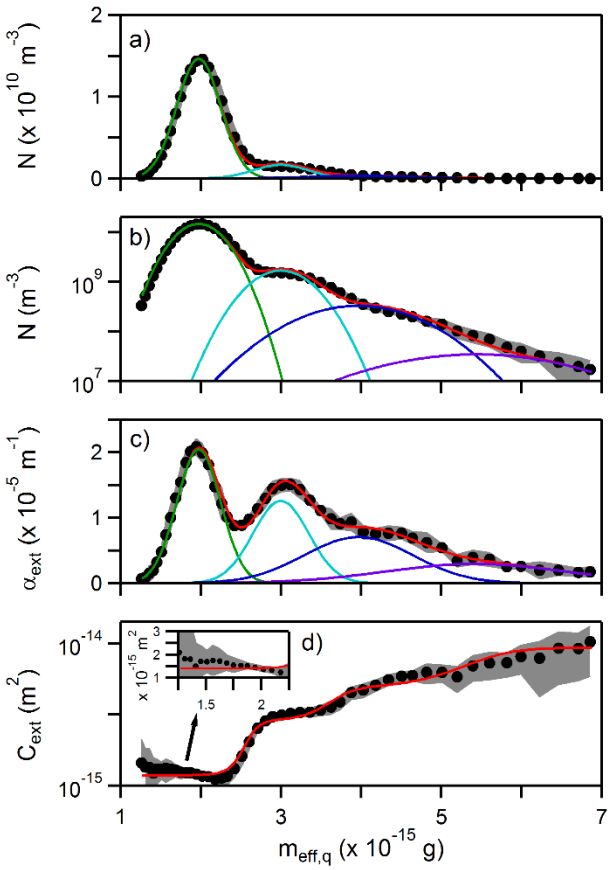

Figure 3: a) Number concentration (N) on linear axis, b) Number concentration (N) on logarithmic axis, c) Extinction (α_{ext}) and d) Extinction cross section (C_{ext}) as a function of particle mass (m_p) for polystyrene latex spheres with a nominal diameter of 147 ± 3 nm. Inset: C_{ext} on a linear axis over the range 1.25 x 10^{-15} g to 2.25 x 10^{-15} g. DMA was set to a D_m = 147 nm. Number concentration plotted on linear and logarithmic axes to highlight peak separation and contribution of $q > +1$, respectively. Solid red, green cyan and blue lines correspond to sum of contributions from all particles and presumably particles with q = +1, +2 and +3, respectively. Measurement uncertainties (2σ) are shown as shaded gray regions.

The number density and extinction as a function of mass exhibit a Gaussian profile as predicted by the convolution of transfer functions (Lall et al. 2009) and can be globally (simultaneously) fit using

$$N = \sum A_{N,q} * \exp\left(\frac{-(m-m_{eff,q})^2}{2\sigma_{eff,q}^2}\right) \text{ and } \alpha_{ext} = \sum A_{\alpha ext,q} * \exp\left(\frac{-(m-m_{eff,q})^2}{2\sigma_{eff,q}^2}\right) \quad (15)$$

where $A_{N,q}$ is the peak number concentration, $A_{\alpha ext,q}$ is the peak extinction, $m_{eff,q}$ is the average effective particle mass and $\sigma_{eff,q}$ is the standard deviation of the distribution; q represents the net particle charge. The summation is included in both of these expressions to account for the presence multiple distributions. PSL fit coefficients are shown in Table 1. The global fit requires that $m_{eff,q}$ and $\sigma_{eff,q}$ are conserved (i.e. the same value for both fits) and as a result, the average extinction cross-section is calculated from the ratio of the amplitudes

$$C_{\mathrm{ext,avg}} = \frac{\int \alpha_{\mathrm{ext,q}} dm_{\mathrm{p}}}{\int N_{\mathrm{q}} dm_{\mathrm{p}}} = \frac{A_{\alpha\mathrm{ext,q}}\sigma_{\mathrm{q}}\sqrt{2\pi}}{A_{\mathrm{N,q}}\sigma_{\mathrm{q}}\sqrt{2\pi}} = \frac{A_{\alpha\mathrm{ext,q}}}{A_{\mathrm{N,q}}} \quad (16)$$

One implicit assumption to the global fit is the treatment of C_{ext} as a constant for particles bearing a specific charge; i.e. C_{ext} does not exhibit a strong dependence on mass over the range of interest. This assumption is acceptable over the mass ranges of interest as a result of transfer function convolution, as the C_{ext} measured at any specific mass, after being sorted by the APM represents the average of particles spanning a finite range of masses, see Fig. 1f and ensuing discussion of AS and soot. This assumption does not hold for strongly scattering spherical particles in the Rayleigh limit as $C_{ext} \approx C_{scat} \propto m_p^2$ since $C_{scat} \propto D_p^6$. This effect can be seen in Fig. S1 for the 102 nm PSL where the fits of the number concentration and extinction are slightly offset from peak center in using Eq. 14. However, although the average masses are slightly offset, the errors introduced to C_{ext} and ρ_{eff} are within 2% for 102 nm PSL particles. We do note that when working with spherical particles, the concentration and extinction could be fit independently as the measured peaks are sufficiently well resolved. However, for consistency we have chosen to retain the global fit for all data sets. For non-spherical particles, the overlap between peaks is significantly higher and the global fit is necessary to properly constrain the center and width between the two distributions (see ensuing discussion on soot).

Fit coefficients for the PSLs with nominal diameters of 102 ± 3 nm, 147 ± 3 nm and 203 ± 5 nm are shown in Table 1. The nominal diameters listed with the dashes correspond to multiplets of PSLs that are able to pass through the DMA with $q > +1$. For the 102 nm PSL, it is expected that the larger particle consists of a triplet of PSLs with $q = +2$ as deduced from $m_{eff,q}$. For the 147 nm PSL, the larger particles are expected to represent a triplet/+2, quartet/+2 and pentet/+2 while for the 203 nm PSLs the larger particles are a triplet/+2 similar to the multiplets observed in (Zelenyuk et al. 2006).

The effective density and extinction cross section of the singlet PSL particles are shown in Table 2. The uncertainties listed with ρ_{eff} represent the width of the distribution ($\sigma_{eff,q}/m_{eff,q}$) to highlight the range of densities observed. These values compare well to the bulk density of polystyrene (1.05 g cm^{-3}). The measured effective densities were higher than the reported bulk density, which may be attributed to surfactant that can remain on the PSL during atomization. The measured C_{ext} were also compared to values calculated using Mie theory for the nominal particle diameters. Good agreement was obtained with the measured values being higher than those calculated. Importantly, for both ρ_{eff} and C_{ext}, the errors from the values for the nominal diameters are within the sizing uncertainty of both the PSLs and the DMA (Kinney et al. 1991; Mulholland et al. 1999).

The PSL mass distribution (and hence transfer function) is broader than theoretically expected from the range of particles transmitted by the DMA. The DMA was set to $Z_p = 1.4010 \times 10^{-8}$ m^2 V^{-1} s^{-1} (147 nm) with $\Delta Z_p = 1.4010 \times 10^{-9}$ m^2 V^{-1} s^{-1} corresponding to particles with D_m of 139 nm to 157 nm being transmitted. The quoted standard deviation for the 147 nm particles is 4.3 nm, so the transfer function of the DMA roughly corresponds to the 2σ width of the PSL distribution. If we assume polystyrene has a uniform density of 1.05 g cm^{-3}, this size range would correspond to masses of 1.48×10^{-15} g to 2.13×10^{-15} g being transmitted by the APM. The actual range of particle masses transmitted by the APM (at $2\sigma_{eff,q}$) is 1.43×10^{-15} g to 2.52×10^{-15} g.

Table 1: Fit coefficients for peaks observed in the mass distribution of PSL nanospheres of 3 nominal diameters

Nominal Diameter (x 10^{-9} m)	$A_{N,q}$ (x 10^{8} m^{-3})	$A_{\alpha ext,q}$ (x 10^{-6} m^{-1})	$m_{eff,q}$ (x 10^{-15} g)	$\sigma_{eff,q}$ (x 10^{-16} g)
102	167 ± 10	2.5 ± 0.1	0.62 ± 0.01	0.88 ± 0.05
--	20 ± 10	2.5 ± 0.2	0.94 ± 0.01	1.0 ± 0.2
147	146 ± 2	20.4 ± 0.3	1.97 ± 0.01	2.74 ± 0.03
--	17 ± 2	13 ± 2	3.00 ± 0.02	3.5 ± 0.3
--	3 ± 2	7 ± 7	4.0 ± 0.2	7 ± 3
--	0.3 ± 2	3 ± 2	5 ± 2	11 ± 13
203	31.8 ± 0.3	29.5 ± 0.3	4.80 ± 0.01	6.8 ± 0.1
--	2.7 ± 0.3	16.4 ± 0.4	7.97 ± 0.04	9.4 ± 0.5

Table 2: Calculated values for q = +1 PSL nanospheres from fit coefficients in Table 1.

Nominal Diameter (x 10^{-9} m)	ρ_{eff} (g cm^{-3})	Error (%)[a]	$C_{ext,calc}$ (x 10^{-15} m^2)	$C_{ext,avg}$ (x 10^{-15} m^2)	Error (%)
102	1.12 ± 0.16	6.4	0.14	0.15 ± 0.02	7
147	1.19 ± 0.16	13	1.26	1.39 ± 0.05	11
203	1.09 ± 0.16	4.3	8.4	9.3 ± 0.3	11

[a] for PSL ρ_{eff} = 1.05 g cm^{-3}

Separation of the individual peaks can be quantified by calculating the peak resolution (R_s):

$$R_s = \frac{2(m_{eff,q2} - m_{eff,q1})}{W_{q2} + W_{q1}} \quad (17)$$

where W is the full peak width and the subscripts $q1$ and $q2$ denote particles with different charges; i.e. +1/+2 or +2/+3; here, W is determined experimentally such that $W = 4\sigma_{eff,q}$ as recommended by (Inczédy et al. 1998) and where $\sigma_{eff,q}$ is the standard deviation from Eq. 15. The peaks are sufficiently resolved when $R_s > 0.5$ when using a CPC alone. For the 102 nm, 147 nm and 203 nm PSLs, the peak resolution of the primary q = +1 peak from the next peak is 0.85, 0.82 and 0.98 indicating the peaks are sufficiently resolved.

4.2. Ammonium sulfate mass distributions

PSL aerosols, in theory, represent the simplest system for DMA-APM separations. However, the presence of aggregates of multiple particles with q > +1 can complicate separation. For polydisperse aerosols, such as ammonium sulfate (AS), the presence of particles with q > +1 can also make separation a challenge. After aerosolization, a 1 mg mL^{-1} AS solution exhibited a lognormal distribution with a geometric mean diameter and geometric standard deviation of 144 nm and 1.61, respectively; a representative size distribution can be seen in Fig. S3a of the Supporting Information. The DMA was set with D_m = 150 nm (Z_p = 1.3661 x 10^{-8} m^2 V^{-1} s^{-1}). A second DMA and charge neutralizer were employed to determine the mobility diameters of particles possessing q > +1 selected by the first DMA and are shown in Fig. S3b. The q = +2 and +3 particles exiting the first DMA have D_m of 234 and 310 nm, respectively.

The APM was scanned across mass space and the corresponding distributions of N (linear), N (logarithmic), α_{ext} and C_{ext} are shown in Figs. 3a through 3d, respectively. As with PSL, number density has been plotted on linear and logarithmic axes to highlight the small absolute contribution to number concentration and the larger relative contribution to extinction by particles bearing higher order charges, respectively. The error bars in the figure correspond to 2σ uncertainty at a 5 s temporal resolution. The data for N and α_{ext} show that for spherical AS, the +2 and +3 charge particles are well separated (Fig. 3b and 3c), similar to the PSLs and the results of (Radney et al. 2013). As with the PSLs, the extinction cross sections (Fig. 3d) of the separated particles possess a continuous slope where particles bearing a unique charge are present; corresponding to the nearly flat sections at $\approx 2.5 \times 10^{-15}$ g, 5×10^{-15} g and 8×10^{-15} g for $q = +1$, +2 and +3, respectively. Where there is overlap between the charges (+1/+2 and +2/+3 at $\approx 4 \times 10^{-15}$ g and 7×10^{-15} g, respectively) there is a sharp change in the slope of C_{ext}, indicative of a transition region with particles of different charges being present.

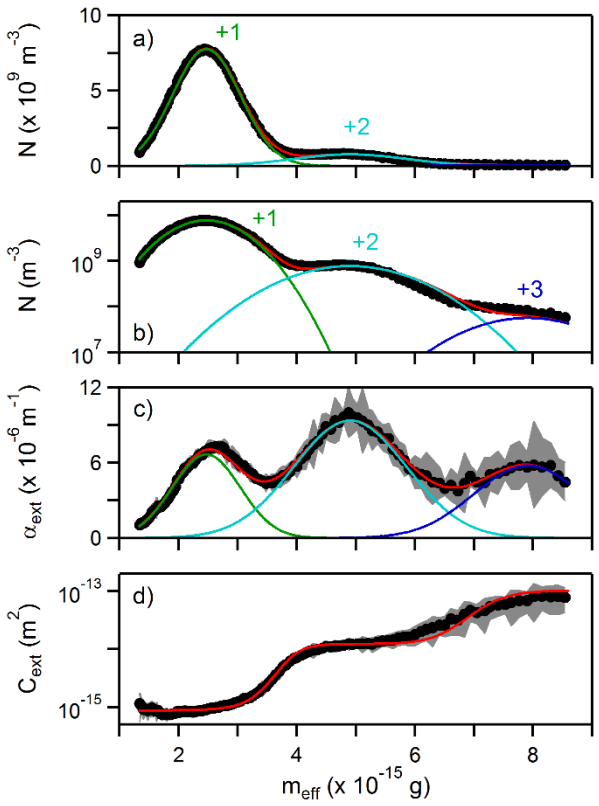

Figure 3: a) Number concentration (N) on linear axis, b) Number concentration (N) on logarithmic axis, c) Extinction (α_{ext}) and d) Extinction cross section (C_{ext}) as a function of particle mass (m_p) for ammonium sulfate with $D_m = 150$ nm. Number concentration plotted on linear and logarithmic axes to highlight peak separation and contribution on $q > +1$ particles, respectively. Solid red, green cyan and blue lines correspond to sum of contributions from all particles and particles with $q = +1$, +2 and +3, respectively. Measurement uncertainties (2σ) are shown as shaded gray regions in c) and d); uncertainties in a) and b) were smaller than data points in the plot and have thus been omitted.

Table 3: Fit coefficients for peaks observed in the mass distribution of D_m = 150 nm AS

q	D_m (x 10^{-9} m)	$A_{N,q}$ (x 10^7 m^{-3})	$A_{\alpha ext,q}$ (x 10^{-6} m^{-1})	$m_{eff,q}$ (x 10^{-15} g)	$\sigma_{eff,q}$ (x 10^{-15} g)
1	150	780 ± 15	6.7 ± 0.2	2.47 ± 0.01	0.58 ± 0.01
2	234	80 ± 15	9.4 ± 0.2	4.90 ± 0.05	0.95 ± 0.05
3	310	6 ± 19	5.8 ± 0.3	7.9 ± 0.1	0.9 ± 0.2

Table 4: Calculated values for D_m = 150 nm AS from the fit coefficients.

q	D_m (x 10^{-9} m)	ρ_{eff} (g cm^{-3})	f_{AS}	n_{eff}	$C_{ext,calc}$ (x 10^{-15} m^2)	$C_{ext,meas}$ (x 10^{-15} m^2)	Error (%)
1	150	1.4 ± 0.3	0.79	1.42	0.76	0.86 ± 0.03	-13
2	234	1.5 ± 0.3	0.83	1.44	10.4	12 ± 2	-17
3	310	1.5 ± 0.2	0.86	1.46	44	100 ± 354	-135

Crystalline AS has a bulk density of 1.77 g cm^{-3}, 21 % higher than the measured ρ_{eff}. The PSL measurements illustrate that the APM and CRD/CPC accurately measured m_p and C_{ext}. Since AS tends to form nearly spherical particles, as demonstrated in (Zelenyuk et al. 2006), we assume that the difference in material density is due to air inclusions within the particle (most likely a result of the rapid and aggressive drying utilized), and the effective refractive index (n_{eff}) can be calculated by volume weighting the corresponding refractive indices; i.e.

$$n_{\mathrm{eff}} = n_{\mathrm{AS}} f_{\mathrm{AS}} + n_{\mathrm{Air}} f_{\mathrm{Air}} = 1.53 * f_{\mathrm{AS}} + 1 * f_{\mathrm{Air}} \quad (18)$$

where n_x, f_x correspond to the refractive index and volume fraction of species x; for AS, n = 1.53 at λ = 660 nm (Toon et al. 1976). The volume fractions, the corresponding n_{eff} and calculated C_{ext} as a function of particle charge can be seen in Table 4. From this weighting, our measurement error of the q = +1 and +2 particles are -13 % and -17 %, respectively. The q = +3 error is -135 % but still within the measurement uncertainty. We note that for q = +3 the uncertainty in C_{ext} is dominated by the uncertainty in the fit of number concentration and not extinction; relative uncertainties are 345 % and 5.4 %, respectively.

Evidence for the convolution of transfer functions between the DMA and APM can be observed upon closer examination of C_{ext}, this corresponds the green lines in Fig. 1a and 1b being multiplied together to obtain the green lines in Fig. 1c and subsequent summation to form the solid red line. For n_{eff} = 1.42 (corresponding to q = +1 in Table 4), increasing D_m from 141 nm to 160 nm (the range of transmitted Z_p) should cause C_{ext} to increase from 5.30 x 10^{-16} m^2 to 1.11 x 10^{-15} m^2, respectively. Instead, C_{ext} has a modest slope with a value of 9 x 10^{-16} m^2 at 1.5 x 10^{-15} g to 1.22 x 10^{-15} m^2 at 3.0 x 10^{-15} g. Over this range of masses the presence of any slope increase is most likely due to the increasing presence of q = +2 particles when $m_p > \approx 2$ x 10^{-15} g.

Like the PSLs, the peaks in the AS distribution are well resolved. The +1/+2 and +2/+3 peaks have R_s of 0.79 and 0.80, respectively. However, as will be shown for soot below, resolution without the optical measurement is not always possible.

4.3. Soot mass distributions

Spherical particles, such as PSLs and AS, offer the most simple case for separation of higher order charges at a selected electrical mobility. For spherical particles, the friction coefficient (f) depends only upon the particle diameter, the Cunningham slip correction factor and gas viscosity as shown in Eq. 2. Aggregates, such as flame generated soot, exhibit more complex friction coefficients. Compared to spherical AS particles with the same volume equivalent diameter (i.e. particles with the same total volume of material), soot particles experience significantly larger drag forces, decreasing the observed m_{eff} for a given Z_p and concomitantly reducing the ability to resolve higher order charges ($q > +1$). This is demonstrated in Fig. 4 where the distribution of fresh ethylene soot from a Santoro diffusion flame (Santoro et al. 1983) at D_m = 150 nm (Z_p = 1.3661 x 10^{-8} m^2 V^{-1} s^{-1}) is shown. The current discussion will focus only on the raw data (black). The fitted and calculated data (colors) will be discussed below. The number concentration data as a function of mass (Fig. 4a) exhibits a non-symmetrical peak shape with a tail extending towards higher mass. The extinction data exhibits a similar non-symmetric peak and an elongated tail of higher mass particles, as evident in Fig. 4b. The tails and shape differences arise from the presence of higher order charges as can be seen from C_{ext} in Fig. 4c. Here, the cross section possesses a single slope up to ≈ 4 x 10^{-16} g indicative of particles with a unique charge. As the mass increases, the slope of C_{ext} rapidly rises due to the presence of $q > +1$ particles within the distribution. Unlike the AS data where the C_{ext} of unique charges was resolved (the stair-step shape of Fig. 3d), for soot the higher order charges in Fig. 4c have been convoluted resulting in the continuous rise of C_{ext}. Upon closer inspection of Fig. 4c, the slope rise in C_{ext} is not constant (i.e. the derivative of the slope ≠ 0), further indicating the presence of particles bearing different charges.

To improve separation, a second CN was employed between the DMA and APM and the mass distribution was re-measured (Fig. 4d – 4f). This serves to reduce the fractional contribution of particles with $q > +1$ in the primary peak and also shifts particles that initially possessed $q > +1$ to now possess $q = +1$ allowing for measurement of m_p instead of m_{eff}. The number concentration (N), extinction (α_{ext}) and extinction cross sections (C_{ext}) are shown in Figs. 4d, 4e, and 4f, respectively. The number concentration data illustrates that the use of a second CN reduces particle counts by nearly an order of magnitude, but also decreases the contribution from $q > +1$ in the primary peak at ≈ 5 x 10^{-16} g. The $q > +1$ reduction is also seen as a shift in the peak mass of α_{ext} from Fig. 4e to 4b. The multiple slopes of C_{ext} in Fig. 4f indicate that the particle distribution still contains higher order charges even with the utilization of multiple CNs. The C_{ext} data also shows that the region where $q = +1$ is isolated is very similar when comparing the use of single CN to two CNs.

Up to this point, we have only commented on the observed shape differences between number concentration, extinction and extinction cross section as a function of mass for soot. We now aim to show how the combination of these measurements allows for both resolving peaks with $R_s < 0.5$ and minimizing uncertainty in m_{eff} and C_{ext} determination. In Fig. 4, the colors green, cyan, and blue correspond to the particles with $q = +1$, +2, and +3, respectively, when exiting the DMA prior to mass selection and are maintained through all plots. In Fig 4d through 4f, the dashed lines are used to indicate that q has changed as a result of the second CN, while the colors have been maintained to correspond to q after the first CN.

The concentration and extinction data shown in Fig. 4d and 4e was fit using Eq. 15 for 6 peaks and the resulting coefficients are shown in Table 5. The values for q and q' in the table represent the particle's charge after the first and second charge neutralizer, respectively. From the fit coefficients, we attempted to globally fit the individual concentration and extinction peaks in Fig. 4a and 4b. Unfortunately, even with pre-constrained fit values for $m_{eff,q}$ and $\sigma_{eff,q}$, unphysical fit coefficients were obtained – N for q = +3 was greater than q = +2 – thus demonstrating that even with the addition of an optical technique peak resolution is not always possible.

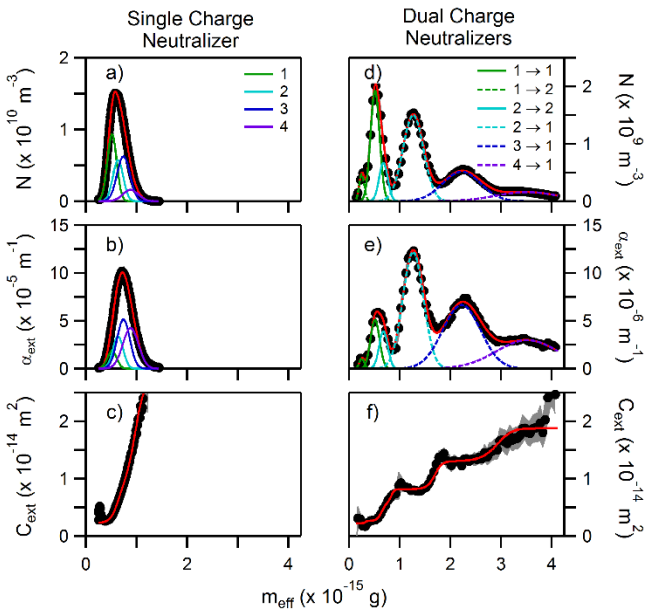

Figure 4: Left column: a) size distribution (dN/dlog(D_m)). b) number concentration, c) extinction (α_{ext}) and d) extinction cross section (C_{ext}) as a function of mass for soot particles with a Z_p = 1.3661 x 10^{-8} m^2 V^{-1} s^{-1} corresponding to a q = +1 D_m of 150 nm using a single charge neutralizer (CN) with a differential mobility analyzer (DMA) and aerosol particle mass analyzer (APM). Right column: same order as the left column except that the particles have been passed through a second charge neutralizer prior to entering the APM causing a redistribution of particle charge. Error bars are 2σ. See discussion in text for additional details.

Table 5: Soot mass distribution fits from Fig. 4f and 4g

q	q'	$A_{N,q}$ (x 10^8 m^{-3})			$A_{\alpha ext,q}$ (x 10^{-6} m^{-1})			$m_{eff,q}$ (x 10^{-15} g)			$\sigma_{eff,q}$ (x 10^{-15} g)			ρ_{eff} (g cm^{-3})			C_{ext} (x 10^{-15} m^2)		
1	2	4.6	±	0.6	0.94	±	0.32	0.25	±	0.01	0.05	±	0.01	0.29	±	0.06	2	±	1
1	1	19	±	1	5.1	±	0.6	0.52	±	0.01	0.09	±	0.01	0.29	±	0.05	2.7	±	0.7
2	2	6	±	2	3.8	±	0.6	0.68	±	0.02	0.09	±	0.01	0.21	±	0.03	6	±	4
2	1	15.0	±	0.3	12.1	±	0.2	1.27	±	0.01	0.20	±	0.01	0.19	±	0.03	8.1	±	0.4
3	1	5.1	±	0.2	6.7	±	0.3	2.22	±	0.02	0.38	±	0.02	0.15	±	0.03	13	±	2
4	1	1.6	±	0.2	3.0	±	0.1	3.53	±	0.06	0.6	±	0.1	0.13	±	0.02	19	±	4

The ability to sufficiently resolve the contribution of every charge has implications for the interpretation of mass and the corresponding optical properties. From Fig. 4b, if we consider the

peak to contain only a single charge and that the tail was a measurement artifact, m_{avg} would be calculated as 5.9 x 10^{-16} g while the measured mass of the resolved q = +1 particle is 5.2 x 10^{-16} g, as determined from the global fit (See Table 5), an error of 13 %. Similarly, if we only consider the extinction at the peak of the distribution, C_{ext} would be calculated as 6.4 x 10^{-15} m^2 while from Table 5 the measured C_{ext} of the isolated q = +1 particle is 2.7 x 10^{-15} m^2, an error of 137 %. Translating these errors to the mass specific extinction cross section (MEC = C_{ext}/m_p), we obtain values of 11 m^2 g^{-1} and 5.1 m^2 g^{-1} for the peak values versus the isolated q = +1 cases, respectively, an error of 110 %, where the error in m_p offsets the error in C_{ext}.

Beyond the limitations in R_s imposed by the particles under investigation, there also exist physical limitations imposed by the APM. In principle, R_s should improve by increasing λ_c; higher λ_c increases the radial versus transversal velocity within the APM thereby narrowing the output mass distribution (decreasing $\sigma_{eff,q}$ in Eq. 15). However, depending upon the flow rate through the APM, the radial travel time may be short relative to the transverse travel time causing σ to approach an asymptotic value. Another consideration for soot at D_m = 150 nm, m_p = 5.1 x 10^{-16} g and the APM rotation speed operates near its physical maximum. Increasing λ_c requires a concomitant increase in rotation speed and is not possible due to instrumentational limitations. The presented data are likely to be universal for other aerosol systems and independent of the instrument utilized. To test this we performed measurements using a larger APM (Kanomax 3600) which has a similar experimental geometry with equivalent results.

5. Conclusions

We have demonstrated practical limits to the DMA-APM separation technique using polystyrene latex nanospheres, ammonium sulfate and lacey soot aggregates and close with a few suggestions for performing DMA-APM measurements based on the presented data:

1. For measurements of non-spherical particles, non-symmetrical mass distributions are a sign of the presence of particles bearing multiple charges. We recommend the use of a second charge neutralizer after the DMA and prior to the APM to aid in the identification and to reduce the effects of particles initially bearing multiple charges.
2. We purposefully chose to collect data at D_m = 150 nm as this represents the worst-case scenario for separation; i.e. the mass separation of the particles is sufficiently small while the probability of having q > +1 is sufficiently large. At smaller D_m, the probability of q > +1 approaches 0, while for larger D_m, the effective mass separation between successive charges is larger.
3. The underlying size distribution of particles will drastically effect the fractional contribution of particles bearing higher charges. If D_m on the rising edge of the distribution are selected (small D_m), than a higher fraction of q > +1 can be expected relative to selecting D_m on the falling edge of the distribution. However, unless methods are taken to physically remove q > +1, there remains a probability, regardless of how small, that q > +1 particles will be present. Further, dilution of the aerosol stream serves to dilute the number concentration of particles as multiple charging is a statistical issue that is independent of concentration.

ACKNOWLEDGEMENTS

We would like to thank the Professor Michael Zachariah laboratory at the University of Maryland for use of a Kanomax 3600 APM. We would also like to thank George Mulholland at NIST and the University of Maryland for a careful and critical review of this manuscript prior to submission.

REFERENCES

Allen, M. D. and Raabe, O. G. (1985). Slip Correction Measurements of Spherical Solid Aerosol Particles in an Improved Millikan Apparatus. *Aerosol Sci. Technol.* 4:269-286.

Atkinson, D. B. (2003). Solving Chemical Problems of Environmental Importance Using Cavity Ring-Down Spectroscopy. *Analyst* 128:117 - 125.

Barone, T. L., Lall, A. A., Storey, J. M. E., Mulholland, G. W., Prikhodko, V. Y., Frankland, J. H., Parks, J. E. and Zachariah, M. R. (2011). Size-Resolved Density Measurements of Particle Emissions from an Advanced Combustion Diesel Engine: Effect of Aggregate Morphology. *Energy Fuels* 25:1978-1988.

Chan, P. and Dahneke, B. (1981). Free-Molecule Drag on Straight Chains of Uniform Spheres. *J. Appl. Phys.* 52:3106-3110.

Charvet, A., Bau, S., Paez Coy, N., Bémer, D. and Thomas, D. (2014). Characterizing the Effective Density and Primary Particle Diameter of Airborne Nanoparticles Produced by Spark Discharge Using Mobility and Mass Measurements (Tandem Dma/Apm). *J. Nanopart. Res.* 16:1-11.

Collins, D. R., Cocker, D. R., Flagan, R. C. and Seinfeld, J. H. (2004). The Scanning Dma Transfer Function. *Aerosol Sci. Technol.* 38:833-850.

Cross, E. S., Onasch, T. B., Ahern, A., Wrobel, W., Slowik, J. G., Olfert, J., Lack, D. A., Massoli, P., Cappa, C. D., Schwarz, J. P., Spackman, J. R., Fahey, D. W., Sedlacek, A., Trimborn, A., Jayne, J. T., Freedman, A., Williams, L. R., Ng, N. L., Mazzoleni, C., Dubey, M., Brem, B., Kok, G., Subramanian, R., Freitag, S., Clarke, A., Thornhill, D., Marr, L. C., Kolb, C. E., Worsnop, D. R. and Davidovits, P. (2010). Soot Particle Studies—Instrument Inter-Comparison—Project Overview. *Aerosol Sci. Technol.* 44:592-611.

Ehara, K., Hagwood, C. and Coakley, K. J. (1996). Novel Method to Classify Aerosol Particles According to Their Mass-to-Charge Ratio—Aerosol Particle Mass Analyser. *J. Aerosol Sci* 27:217-234.

Geller, M., Biswas, S. and Sioutas, C. (2006). Determination of Particle Effective Density in Urban Environments with a Differential Mobility Analyzer and Aerosol Particle Mass Analyzer. *Aerosol Sci. Technol.* 40:709-723.

Gopalakrishnan, R., Thajudeen, T. and Hogan, C. J. (2011). Collision Limited Reaction Rates for Arbitrarily Shaped Particles across the Entire Diffusive Knudsen Number Range. *The Journal of Chemical Physics* 135:054302.

Hogan, C. J., Jr. and de la Mora, J. F. (2011). Ion Mobility Measurements of Nondenatured 12–150 kda Proteins and Protein Multimers by Tandem Differential Mobility Analysis–Mass Spectrometry (Dma-Ms). *J. Am. Soc. Mass. Spectrom.* 22:158-172.

Inczédy, J., Lengyel, T. and Ure, A. M. (1998). *Iupac Analytical Chemistry Division, Compendium of Analytical Nomenclature (the Iupac 'Orange Book')*. Blackwell Science, Ltd., Oxford, UK.

Isella, L. and Drossinos, Y. (2010). Langevin Agglomeration of Nanoparticles Interacting Via a Central Potential. *Phys. Rev. E: Stat. Phys., Plasmas, Fluids,* 82:011404.

Kinney, P. D., Pui, D. Y. H., Mulholland, G. W. and Bryner, N. P. (1991). Use of the Electrostatic Classification Method to Size 0.1 Mm Particles - a Feasibility Study. *J. Res. Natl. Inst. Stand. Technol.* 96:147 - 176.

Knutson, E. O. and Whitby, K. T. (1975). Aerosol Classification by Electric Mobility: Apparatus, Theory, and Applications. *J. Aerosol Sci* 6:443-451.

Kuwata, M. (2015). Particle Classification by the Tandem Differential Mobility Analyzer–Particle Mass Analyzer System. *Aerosol Sci. Technol.* 49:508-520.

Kuwata, M. and Kondo, Y. (2009). Measurements of Particle Masses of Inorganic Salt Particles for Calibration of Cloud Condensation Nuclei Counters. *Atmos. Chem. Phys. Discuss.* 9:4653-4689.

Laborde, M., Mertes, P., Zieger, P., Dommen, J., Baltensperger, U. and Gysel, M. (2012). Sensitivity of the Single Particle Soot Photometer to Different Black Carbon Types. *Atmos. Meas. Tech.* 5:1031-1043.

Lall, A. A., Ma, X., Guha, S., Mulholland, G. W. and Zachariah, M. R. (2009). Online Nanoparticle Mass Measurement by Combined Aerosol Particle Mass Analyzer and Differential Mobility Analyzer: Comparison of Theory and Measurements. *Aerosol Sci. Technol.* 43:1075-1083.

Lall, A. A., Rong, W., Mädler, L. and Friedlander, S. K. (2008). Nanoparticle Aggregate Volume Determination by Electrical Mobility Analysis: Test of Idealized Aggregate Theory Using Aerosol Particle Mass Analyzer Measurements. *J. Aerosol Sci* 39:403-417.

Lee, S. Y., Chang, H., Ogi, T., Iskandar, F. and Okuyama, K. (2011). Measuring the Effective Density, Porosity, and Refractive Index of Carbonaceous Particles by Tandem Aerosol Techniques. *Carbon* 49:2163-2172.

Lee, S. Y., Widiyastuti, W., Tajima, N., Iskandar, F. and Okuyama, K. (2009). Measurement of the Effective Density of Both Spherical Aggregated and Ordered Porous Aerosol Particles Using Mobility- and Mass-Analyzers. *Aerosol Sci. Technol.* 43:136-144.

Lin, G.-Y., Liao, B.-X., Tzeng, N.-J., Chen, C.-W., Uang, S.-N., Chen, S.-C., Pui, D. Y. H. and Tsai, C.-J. (2014). The Effect of Nanoparticle Convection-Diffusion Loss on the Transfer Function of an Aerosol Particle Mass Analyzer. *Aerosol Sci. Technol.* 48:583-592.

Ma, X., Zangmeister, C. D., Gigault, J., Mulholland, G. W. and Zachariah, M. R. (2013a). Soot Aggregate Restructuring During Water Processing. *J. Aerosol Sci* 66:209-219.

Ma, X., Zangmeister, C. D. and Zachariah, M. R. (2013b). Soot Oxidation Kinetics: A Comparison Study of Two Tandem Ion-Mobility Methods. *J. Phys. Chem. C* 117:10723-10729.

Mackowski, D. W. (2006). Monte Carlo Simulation of Hydrodynamic Drag and Thermophoresis of Fractal Aggregates of Spheres in the Free-Molecule Flow Regime. *J. Aerosol Sci* 37:242-259.

Malloy, Q. G. J., Nakao, S., Qi, L., Austin, R., Stothers, C., Hagino, H. and Cocker, D. R. (2009). Real-Time Aerosol Density Determination Utilizing a Modified Scanning Mobility Particle Sizer—Aerosol Particle Mass Analyzer System. *Aerosol Sci. Technol.* 43:673-678.

McMurry, P. H., Wang, X., Park, K. and Ehara, K. (2002). The Relationship between Mass and Mobility for Atmospheric Particles: A New Technique for Measuring Particle Density. *Aerosol Sci. Technol.* 36:227-238.

Meakin, P., Donn, B. and Mulholland, G. W. (1989). Collisions between Point Masses and Fractal Aggregates. *Langmuir* 5:510-518.

Melas, A. D., Isella, L., Konstandopoulos, A. G. and Drossinos, Y. (2014). Friction Coefficient and Mobility Radius of Fractal-Like Aggregates in the Transition Regime. *Aerosol Sci. Technol.* 48:1320-1331.

Mulholland, G. W., Bryner, N. P. and Croarkin, C. (1999). Measurement of the 100 Nm Nist Srm 1963 by Differential Mobility Analysis. *Aerosol Sci. Technol.* 31:39-55.

Olfert, J. S. (2005). A Numerical Calculation of the Transfer Function of the Fluted Centrifugal Particle Mass Analyzer. *Aerosol Sci. Technol.* 39:1002-1009.

Olfert, J. S. and Collings, N. (2005). New Method for Particle Mass Classification—the Couette Centrifugal Particle Mass Analyzer. *J. Aerosol Sci* 36:1338-1352.

Olfert, J. S., Reavell, K. S., Rushton, M. G. and Collings, N. (2006). The Experimental Transfer Function of the Couette Centrifugal Particle Mass Analyzer. *J. Aerosol Sci* 37:1840-1852.

Pagels, J., Khalizov, A. F., McMurry, P. H. and Zhang, R. Y. (2009). Processing of Soot by Controlled Sulphuric Acid and Water Condensation—Mass and Mobility Relationship. *Aerosol Sci. Technol.* 43:629-640.

Park, K., Cao, F., Kittelson, D. B. and McMurry, P. H. (2003a). Relationship between Particle Mass and Mobility for Diesel Exhaust Particles. *Environ. Sci. Technol.* 37:577-583.

Park, K., Kittelson, D. and McMurry, P. (2004a). Structural Properties of Diesel Exhaust Particles Measured by Transmission Electron Microscopy (Tem): Relationships to Particle Mass and Mobility. *Aerosol Sci. Technol.* 38:881-889.

Park, K., Kittelson, D., Zachariah, M. and McMurry, P. (2004b). Measurement of Inherent Material Density of Nanoparticle Agglomerates. *J. Nanopart. Res.* 6:267-272.

Park, K., Kittelson, D. B. and McMurry, P. H. (2003b). A Closure Study of Aerosol Mass Concentration Measurements: Comparison of Values Obtained with Filters and by Direct Measurements of Mass Distributions. *Atmos. Environ.* 37:1223-1230.

Radney, J. G., Ma, X., Gillis, K. A., Zachariah, M. R., Hodges, J. T. and Zangmeister, C. D. (2013). Direct Measurements of Mass-Specific Optical Cross Sections of Single Component Aerosol Mixtures. *Anal. Chem.* 85:8319-8325.

Radney, J. G., You, R., Ma, X., Conny, J. M., Zachariah, M. R., Hodges, J. T. and Zangmeister, C. D. (2014). Dependence of Soot Optical Properties on Particle Morphology: Measurements and Model Comparisons *Environ. Sci. Technol.* 48:3169 - 3176.

Rissler, J., Messing, M. E., Malik, A. I., Nilsson, P. T., Nordin, E. Z., Bohgard, M., Sanati, M. and Pagels, J. H. (2013). Effective Density Characterization of Soot Agglomerates from Various Sources and Comparison to Aggregation Theory. *Aerosol Sci. Technol.* 47:792-805.

Sakurai, H., Park, K., McMurry, P. H., Zarling, D. D., Kittelson, D. B. and Ziemann, P. J. (2003). Size-Dependent Mixing Characteristics of Volatile and Nonvolatile Components in Diesel Exhaust Aerosols. *Environ. Sci. Technol.* 37:5487-5495.

Santoro, R. J., Semerjian, H. G. and Dobbins, R. A. (1983). Soot Particle Measurements in Diffusion Flames. *Combust. Flame* 51:203-218.

Scheckman, J. H., McMurry, P. H. and Pratsinis, S. E. (2009). Rapid Characterization of Agglomerate Aerosols by in Situ Mass−Mobility Measurements. *Langmuir* 25:8248-8254.

Shin, W. G., Mulholland, G. W., Kim, S. C., Wang, J., Emery, M. S. and Pui, D. Y. H. (2009). Friction Coefficient and Mass of Silver Agglomerates in the Transition Regime. *J. Aerosol Sci* 40:573-587.

Shin, W. G., Mulholland, G. W. and Pui, D. Y. H. (2010). Determination of Volume, Scaling Exponents, and Particle Alignment of Nanoparticle Agglomerates Using Tandem Differential Mobility Analyzers. *J. Aerosol Sci* 41:665-681.

Sullivan, D. B., Allan, D. W., Howe, D. A. and Walls, F. L. (1990). Characterization of Clocks and Oscillators. *NIST Tech. Note 1337*:1-342.

Sultanovaa, N., Kasarovaa, S. and Nikolov, I. (2009). Dispersion Properties of Optical Polymers. *Acta Phys. Pol., A* 116:585 - 587.

Tajima, N., Fukushima, N., Ehara, K. and Sakurai, H. (2011). Mass Range and Optimized Operation of the Aerosol Particle Mass Analyzer. *Aerosol Sci. Technol.* 45:196-214.

Tajima, N., Sakurai, H., Fukushima, N. and Ehara, K. (2013). Design Considerations and Performance Evaluation of a Compact Aerosol Particle Mass Analyzer. *Aerosol Sci. Technol.* 47:1152-1162.

Toon, O. B., Pollack, J. B. and Khare, B. N. (1976). The Optical Constants of Several Atmospheric Aerosol Species: Ammonium Sulfate, Aluminum Oxide, and Sodium Chloride. *J. Geophys. Res.* 81:5733-5748.

Wiedensohler, A., Birmili, W., Nowak, A., Sonntag, A., Weinhold, K., Merkel, M., Wehner, B., Tuch, T., Pfeifer, S., Fiebig, M., Fjäraa, A. M., Asmi, E., Sellegri, K., Depuy, R., Venzac, H., Villani, P., Laj, P., Aalto, P., Ogren, J. A., Swietlicki, E., Williams, P., Roldin, P., Quincey, P., Hüglin, C., Fierz-Schmidhauser, R., Gysel, M., Weingartner, E., Riccobono, F., Santos, S., Grüning, C., Faloon, K., Beddows, D., Harrison, R., Monahan, C., Jennings, S. G., O'Dowd, C. D., Marinoni, A., Horn, H. G., Keck, L., Jiang, J., Scheckman, J., McMurry, P. H., Deng, Z., Zhao, C. S., Moerman, M., Henzing, B., de Leeuw, G., Löschau, G. and Bastian, S. (2012). Mobility Particle Size Spectrometers: Harmonization of Technical Standards and Data Structure to Facilitate High Quality Long-Term Observations of Atmospheric Particle Number Size Distributions. *Atmos. Meas. Tech.* 5:657-685.

Wiedensohler, A. and Fissan, H. J. (1988). Aerosol Charging in High Purity Gases. *J. Aerosol Sci* 19:867-870.

Xue, H., Khalizov, A. F., Wang, L., Zheng, J. and Zhang, R. (2009). Effects of Coating of Dicarboxylic Acids on the Mass−Mobility Relationship of Soot Particles. *Environ. Sci. Technol.* 43:2787-2792.

Zelenyuk, A., Cai, Y. and Imre, D. (2006). From Agglomerates of Spheres to Irregularly Shaped Particles: Determination of Dynamic Shape Factors from Measurements of Mobility and Vacuum Aerodynamic Diameters. *Aerosol Sci. Technol.* 40:197-217.

Zhang, C., Thajudeen, T., Larriba, C., Schwartzentruber, T. E. and Hogan, C. J. (2012). Determination of the Scalar Friction Factor for Nonspherical Particles and Aggregates across the Entire Knudsen Number Range by Direct Simulation Monte Carlo (Dsmc). *Aerosol Sci. Technol.* 46:1065-1078.